



Highly efficient visible-light-driven photocatalytic degradation of VOCs by CO₂-assisted synthesized mesoporous carbon confined mixed-phase TiO₂ nanocomposites derived from MOFs

Hongli Liu, Yaping Ma, Jiangyao Chen, Meicheng Wen, Guiying Li, Taicheng An*

Guangzhou Key Laboratory of Environmental Catalysis and Pollution Control, Guangdong Key Laboratory of Environmental Catalysis and Health Risk Control, School of Environmental Science and Engineering, Institute of Environmental Health and Pollution Control, Guangdong University of Technology, Guangzhou 510006, China

ARTICLE INFO

Keywords:

TiO₂@C-N nanocomposites
Photocatalytic degradation
Volatile organic compounds
Metal organic framework
Pyrolysis

ABSTRACT

Improving the visible light response and efficient separation of electron-hole pairs play vital roles in commonly used TiO₂ photocatalyst for VOCs degradation. Herein, N-doped mesoporous carbon encapsulated anatase-rutile phase junction TiO₂ (TiO₂@C-N(x)) was successfully synthesized via the pyrolysis of a representative amine functionalized Ti-based MOF, NH₂-MIL-125, under the atmosphere of Ar and subsequent CO₂ treatment. Our synthesis strategy was based on the rational regulation of the formation of TiO₂ phase junction and the decomposition of amorphous carbon onto the TiO₂@C-N (without subsequent CO₂ process) using CO₂ as both anatase-rutile phase transformation promoter and mild oxidant. Compared with TiO₂@C-N, TiO₂@C-N(x) nanocomposites with subsequent CO₂ process exhibit significantly improved photocatalytic activity as well as mineralization efficiencies. For example, the mineralization efficiency reached 51.9% at 62.4% of styrene degradation within 240 min of visible-light irradiation by using the optimal TiO₂@C-N(30) nanocomposites as compared with only 19.7% mineralization efficiency at 31.0% of styrene degradation under the same conditions of TiO₂@C-N. Furthermore, the primary radicals involved in degradation of VOCs was identified by electron paramagnetic resonance spectroscopy, and the possible degradation intermediates were also monitored by means of proton transfer reaction time-of-flight mass spectrometry (PTR-ToF-MS). Finally, the radicals involved degradation reaction mechanism was also tentatively proposed.

1. Introduction

Volatile organic compounds (VOCs), as an important group of pollutants in air, have imposed adverse effects on ecological environment and human health due to its toxicity and environmental persistence [1,2]. Semiconductor photocatalytic oxidation which has great potential to degrade a large variety of VOCs into innocuous CO₂ and H₂O under light illumination has been regarded as an attractive technology to alleviate the above issues [3–11]. In this regard, TiO₂ is one of the most extensively investigated and highly promising photocatalysts due to its earth abundance, low cost, excellent stability and relatively strong oxidative ability power [4–11]. Despite these advantages, the wide band gap (~3.2 eV), weak adsorption of reactants and fast recombination of electron-hole of nanosized TiO₂ often result in poor visible light response (only 5% of solar light) and low efficiency [5], which significantly hamper its feasible application for photocatalytic removal of VOCs. To address these issues, the development of a TiO₂-

based photocatalyst that combines excellent visible light absorption, large surface area and efficient electron-hole separation would be highly desirable, but exceedingly challenging.

Recently, phase junction TiO₂ with same chemical composition but different crystal structure has sparked much attention to boost the photocatalytic performance [12–17]. As a typical example, Degussa P25 composed of 80% anatase and 20% rutile phases usually exhibited higher photocatalytic activity compared with its pure anatase or rutile counterparts. It was also demonstrated that the formation of TiO₂ phase junction by appropriate alignment of anatase and rutile phase was responsible for the improved photocatalytic activity because the phase junction at the interface can be beneficial to accelerate the charge transfer and thus reduce the electron-hole recombination rate [12–16]. However, its low surface area and weak visible light activity make it still difficult to achieve satisfactory efficiency. On the other hand, due to the large surface area, excellent light harvesting and superior electronic conductivity, the integration of TiO₂ with graphitic carbon is

* Corresponding author.

E-mail address: antc99@gdut.edu.cn (T. An).



considered as an alternative strategy to improve the photocatalytic activity [18–24]. This combination could not only enhance the VOCs adsorption capacity to increase the degradation chances due to large surface area, but also be likely to offer fast electron transfer channel to prevent the recombination of photogenerated electron-hole pairs. In particular, N-doping graphitic carbon can expand the light absorption region from UV to visible light while maintaining their outstanding properties [18,19]. Unfortunately, traditional photocatalysts assembled simply from TiO_2 or its precursors with graphitic carbon frequently suffer from the weak interfacial contact and long electron transport distance between graphitic carbon and TiO_2 , leading limited electron-hole separation [20,25]. To maximize the photocatalytic performance, it is indispensable to explore an efficient strategy to integrate both the merits of the anatase and rutile phase junction TiO_2 with N-doping graphitic carbon.

Metal-organic frameworks (MOFs) are an emerging family of porous materials constructed from inorganic metal ions and organic ligands through coordination bonding [26,27]. Recently, MOFs have proved to be an ideal platform for synthesizing a variety of carbon confined metal oxide or metal nanoparticles because the metal nodes and organic ligands in MOFs can be *in situ* transformed to metal oxide or metal nanoparticles and porous carbon depending on the matrix MOF structure and pyrolysis conditions [28–30]. The resulting nanocomposites are able to partly inherit the intriguing structural features of parent MOFs, including large surface area, uniform heteroatom doping (e.g., N, S), highly dispersed active sites and controllable compositions [28,29,31–33]. More importantly, obviously different from previous methods involving TiO_2 or its precursors deposited onto carbon, the coordination bondings between metal nodes and organic ligands in MOFs are capable of providing strong interactions between the *in situ* formed metal oxide and carbon during the pyrolysis process, which would guarantee the excellent interfacial contact. Additionally, it has demonstrated that the phase transformation between anatase and rutile TiO_2 can occur by adjusting the reducibility and oxidizability of the calcination atmosphere [34,35]. Therefore, accurate selection of MOF and its pyrolysis conditions could obtain N-doped mesoporous carbon confined anatase-rutile phase junction TiO_2 ($\text{TiO}_2@\text{C-N}(\text{x})$) with well synergistic effects and gain optimal photocatalytic performance for VOCs efficient degradation.

Bearing the aforementioned considerations in mind, a facile synthetic strategy was developed to achieve $\text{TiO}_2@\text{C-N}(\text{x})$ nanocomposites by direct pyrolysis of a representative amine functionalized Ti-based MOF, $\text{NH}_2\text{-MIL-125}$, under the treatment of Ar and subsequent CO_2 atmosphere. Interestingly, simultaneous control over the ratio of anatase-rutile TiO_2 and surface properties of carbon shell were acquired by the use of CO_2 as both phase transformation agent and mild oxidant. Moreover, the introduction of CO_2 could enlarge the existing pores and even create new pore by oxidative decomposition of the amorphous carbon derived from MOF under Ar atmosphere while the more stable graphitic carbon would be retained. Such regulations were conducive to accelerate the electron transfer and shorten the transport distance between the photogenerated carriers and reactants, leading to efficient photogenerated electron-hole separation and then improved photocatalytic activity. Remarkably, the $\text{TiO}_2@\text{C-N}(\text{x})$ nanocomposites with CO_2 treatment exhibited extraordinary high photocatalytic efficiencies and the mineralization efficiency.

2. Experimental section

2.1. Chemicals

Tetrapropyl orthotitanate (98%, $\text{Ti-(OC}_3\text{H}_7)_4$), 2-aminoterephthalic acid (98%), 5,5-dimethyl-1-pyrroline N-oxide (DMPO) were purchased from J&K Scientific Ltd. Methanol (A.R.), *N,N*-dimethylformamide (A.R.) and styrene (A.R.) were purchased from Sinopharm Chemical reagent Co., Ltd. and used without any purification.

2.2. Materials synthesis

2.2.1. Synthesis of $\text{NH}_2\text{-MIL-125}$

$\text{NH}_2\text{-MIL-125}$ was prepared by a solvothermal method according to the previously reported procedures [36]. Briefly, tetrapropyl orthotitanate (2.4 mL), 2-aminoterephthalic acid (2.2 g), DMF (36 mL) and methanol (4.0 mL) were loaded into a 100 mL Teflon-lined stainless-steel autoclave. Then, the resulting mixture was heated at 150 °C for 48 h. After cooling down to room temperature, the formed solid was collected by filtration, followed by washing several times with DMF and methanol. Finally, the as-prepared powder was dried under vacuum at 150 °C for 12 h to obtain activated $\text{NH}_2\text{-MIL-125}$.

2.2.2. Synthesis of $\text{TiO}_2@\text{C-N}(\text{x})$

Typically, 1 g of activated $\text{NH}_2\text{-MIL-125}$ was annealed at 600 °C for 6 h under Ar atmosphere with a ramp rate of 1 °C min⁻¹, and then cooled down to room temperature to obtain $\text{TiO}_2@\text{C-N}$ sample. For the $\text{TiO}_2@\text{C-N}(\text{x})$ samples, 1 g of activated $\text{NH}_2\text{-MIL-125}$ was annealed at 600 °C for 6 h under Ar atmosphere with a ramp rate of 1 °C min⁻¹. Subsequently, the sample was first cooled down to 500 °C and further annealed at 500 °C for a certain time (30, 60 and 90 min) in CO_2 atmosphere to gain $\text{TiO}_2@\text{C-N}(\text{x})$ samples, where x indicated the annealing time under CO_2 atmosphere.

2.3. Characterization

Powder X-ray diffraction (XRD) patterns were conducted on a D/MAX-Ultima IV with Cu K α radiation operating at 40 kV and 40 mA. Raman spectra were collected on a LabRAM HR800 Raman Spectroscopy (HORIBA Jobin Yvon). N_2 adsorption-desorption isotherms were recorded on a Micromeritics ASAP2020 M at 77 K after the samples were degassed under vacuum at 120 °C for 12 h. UV-vis diffuse reflectance spectra were obtained by an Agilent Carry 300 spectrophotometer in the wavelength range of 200–800 nm with BaSO_4 as a standard reference. The size, morphology, and microstructure of $\text{TiO}_2@\text{C-N}$ and $\text{TiO}_2@\text{C-N}(\text{x})$ samples were observed by using a JEM-2010 F transmission electron microscopy with operating voltage at 200 kV. Before analysis, the analyzed sample was dispersed into ethanol and directly dropped onto a copper-supported perforated carbon film. The scanning electron microscopic (SEM) images were carried out on a Zeiss Merlin instrument. X-ray photoelectron spectroscopy (XPS) analyses were performed with an ultra-high vacuum multipurpose surface analysis system (Escalab 250Xi, Thermo Fisher). Binding energies were referenced to the C1 s line at 284.8 eV from adventitious carbon. Elemental analysis was obtained with an Elementar Vario EL III equipment by weighing samples of 0.2–0.3 mg and packing with aluminum foil for the measurement.

2.4. Photoelectrochemical measurements of prepared nanocomposites

Photoelectrochemical properties were also measured using a CHI 600E electrochemical workstation (Chenhua Instrument, China) with a standard three-electrode system. The Ag/AgCl and Pt foil serve as the reference and counter electrodes, respectively. The working electrode was $\text{TiO}_2@\text{C-N}$ or $\text{TiO}_2@\text{C-N}(\text{x})$ coated FTO glass, and 0.5 M Na_2SO_4 aqueous solution was utilized as electrolyte. A 300 W Xe lamp with a UV cutoff filter (> 420 nm) was employed as light source. For the preparation of working electrode, 10 mg of activated $\text{TiO}_2@\text{C-N}$ or $\text{TiO}_2@\text{C-N}(\text{x})$ sample was dispersed into 0.5 mL ethanol and ultrasonicated for 20 min. Subsequently, the suspension was dropped onto the conductive side of the FTO glass substrate and further dried to remove the organic residuals. The photocurrent signals of the samples were tested at a 0.5 V chopped light. The electrochemical impedance spectroscopy (EIS) was also recorded in the frequency range between 1 and 10⁵ Hz with a bias potential of 1.0 V.

2.5. Photocatalytic degradation and intermediates identification experiments

The photocatalytic activities of the synthesized samples were assessed in our custom-made cubic quartz glass reactor [4] by the degradation of gaseous styrene under ambient conditions. A 300 W xenon lamp was chosen as a light source and was assembled at the top of the reactor with the distance of 10 cm. Typically, 0.08 g of $\text{TiO}_2@\text{C-N}$ or $\text{TiO}_2@\text{C-N(x)}$ sample was filled into the reactor. Subsequently, gaseous styrene with a constant inlet concentration of $35 \pm 1 \text{ ppmv}$ balanced by air was introduced into the reactor with a flow rate of 60 mL min^{-1} . Before the irradiation, the sample was maintained in the dark to establish a gas-solid adsorption-desorption equilibrium. The concentrations of remaining styrene and formed CO_2 in the effluent gas were determined by using online gas chromatograph with two flame ionization detector (FID), respectively. Electron paramagnetic resonance (EPR) spectrometer (EMXPlus-10/12, Bruker) were also employed to further characterize the generated $\cdot\text{OH}^-$ and $\cdot\text{O}^{2-}$ radicals trapped by DMPO in these photocatalytical systems when different photocatalysts were employed to degrade gaseous styrene under visible light irradiation.

The possible degradation intermediates were identified and monitored by a commercial PTR-ToF-MS 1000 (Ionicon Analytik GmbH, Austria) in its standard configuration. The measurement was based on proton transfer processes involving hydronium ion (H_3O^+), which could ionize VOCs in non-dissociative formalization to produce molecular ionic species according to the references [37–39]. The gas from the photocatalytic reaction system was introduced into the reaction drift tube via 1.5 m long heated (at 80°C) PEEK tubing with a flow rate of approximately 30 mL min^{-1} . The key factors of the drift tube conditions were as following: drift pressure of 2.30 mbar, 80°C and voltage at 600 V, corresponding to E/N ratio approximately 130 Td ($1 \text{ Td} = 10^{-17} \text{ V cm}^2$). Then, these species were detected by the MS system and were identified.

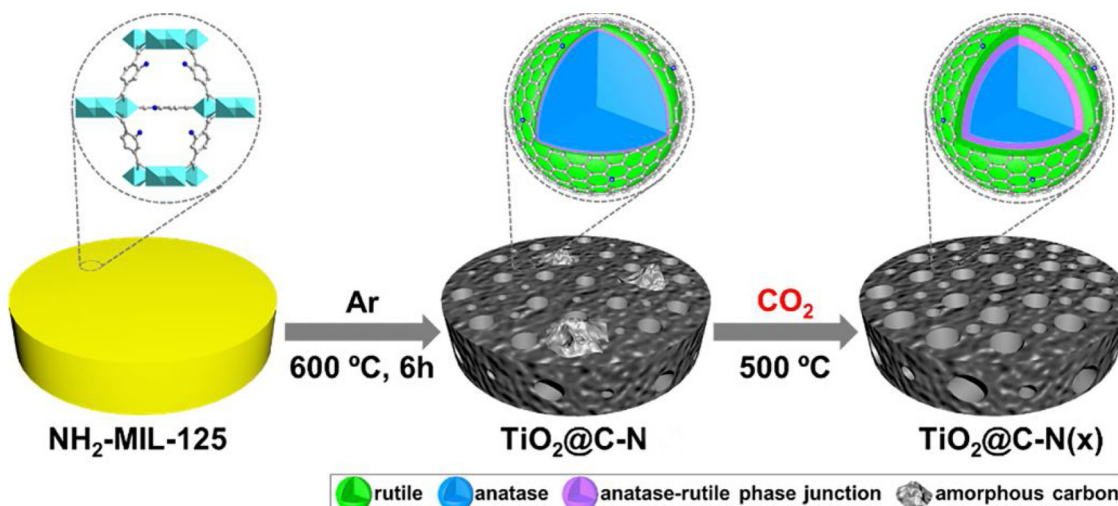
3. Results and discussion

3.1. Characterization of photocatalysts

In this work, N-doped mesoporous carbon encapsulated anatase-rutile phase junction TiO_2 was synthesized by direct pyrolysis of $\text{NH}_2\text{-MIL-125}$ under Ar and subsequent treatment of CO_2 , and the synthesis strategy was illustrated in Scheme 1. The crystallographic structure of the $\text{NH}_2\text{-MIL-125}$, $\text{TiO}_2@\text{C-N}$ and $\text{TiO}_2@\text{C-N(x)}$ samples was examined by the XRD patterns. As showed in Fig. S1, the XRD peaks of the as-

synthesized $\text{NH}_2\text{-MIL-125}$ matched well with the simulated XRD patterns, demonstrating the formation of pure phase $\text{NH}_2\text{-MIL-125}$. After the pyrolysis of $\text{NH}_2\text{-MIL-125}$, the XRD patterns of $\text{TiO}_2@\text{C-N}$ and $\text{TiO}_2@\text{C-N(x)}$ were displayed in Fig. 1a. It is clear to see that the characteristic peaks at 2θ of 25.28° , 37.8° , 48.05° , 53.89° , 55.06° , 62.69° and 70.3° could be indexed to the (101), (004), (200), (105), (211), (204) and (220) crystal planes of anatase TiO_2 (JCPDS 21-1272), respectively. Meanwhile, the diffraction peaks around 27.4° , 36.08° , 39.17° , 54.33° and 62.74° corresponding to the (110), (101), (200), (211) and (002) crystal planes of rutile TiO_2 (JCPDS 21-1276) were also observed in the $\text{TiO}_2@\text{C-N}$ and all the $\text{TiO}_2@\text{C-N(x)}$ samples, demonstrating that the synthesized samples consisted of two phases with anatase and rutile TiO_2 . Moreover, the relative ratio of the rutile and anatase phase in $\text{TiO}_2@\text{C-N(x)}$ samples gradually increased with prolonging the annealing time in CO_2 atmosphere (Fig. S2), which indicated that the annealing step could be considered as a feasible way to regulate the phase composition to form anatase-rutile phase junction by accurately control the CO_2 treatment conditions. Nevertheless, no obvious characteristic diffraction peaks of carbons were observed for all the $\text{TiO}_2@\text{C-N(x)}$ samples, potentially due to the presence of the tight bonding between the carbon and TiO_2 during the annealing processes [40].

The crystal structure and composition of $\text{TiO}_2@\text{C-N}$ and $\text{TiO}_2@\text{C-N(x)}$ samples were further validated by Raman spectroscopy. As Fig. 1b shows, the Raman spectra of $\text{TiO}_2@\text{C-N}$ exhibited clear peaks at 155 , 201.2 , 396.8 , 509.2 and 631.8 cm^{-1} , which were assigned as the typical E_g , E_g , B_{1g} , A_{1g} , and E_g vibrational modes of the anatase phase, respectively, based on previous references [41,42]. It is known that the intrinsic Raman peaks of rutile TiO_2 center at 245 , 442 , and 607 cm^{-1} , respectively [42–44]. However, for the $\text{TiO}_2@\text{C-N}$ sample, no identifiable peaks associated with rutile TiO_2 were observed, possibly due to the low content of rutile phase compared with anatase phase. This result was supported by the XRD results showed as before (Figs. 1a and S2). After annealing in CO_2 atmosphere, a typical rutile peak at 251.8 cm^{-1} appeared and the intensity became much stronger with increasing the time of CO_2 annealing. Meanwhile, the peaks at 201.2 and 396.8 cm^{-1} apparently shifted to higher Raman frequencies and the peaks at 631.8 cm^{-1} also shifted to lower Raman frequencies with the increase of CO_2 annealing time. Moreover, the peaks intensity of B_{1g} and E_g became much stronger while the peak at the wavelength of 509.2 cm^{-1} gradually disappeared. These observations suggested a clear coexistence of anatase and rutile phases in the $\text{TiO}_2@\text{C-N(x)}$ samples and an increased ratio of the rutile phase was observed with prolonging the annealing time in CO_2 atmosphere, consisted with our above mentioned XRD measurements.



Scheme 1. Illustration of the preparation strategy of $\text{TiO}_2@\text{C-N(x)}$ nanocomposites.

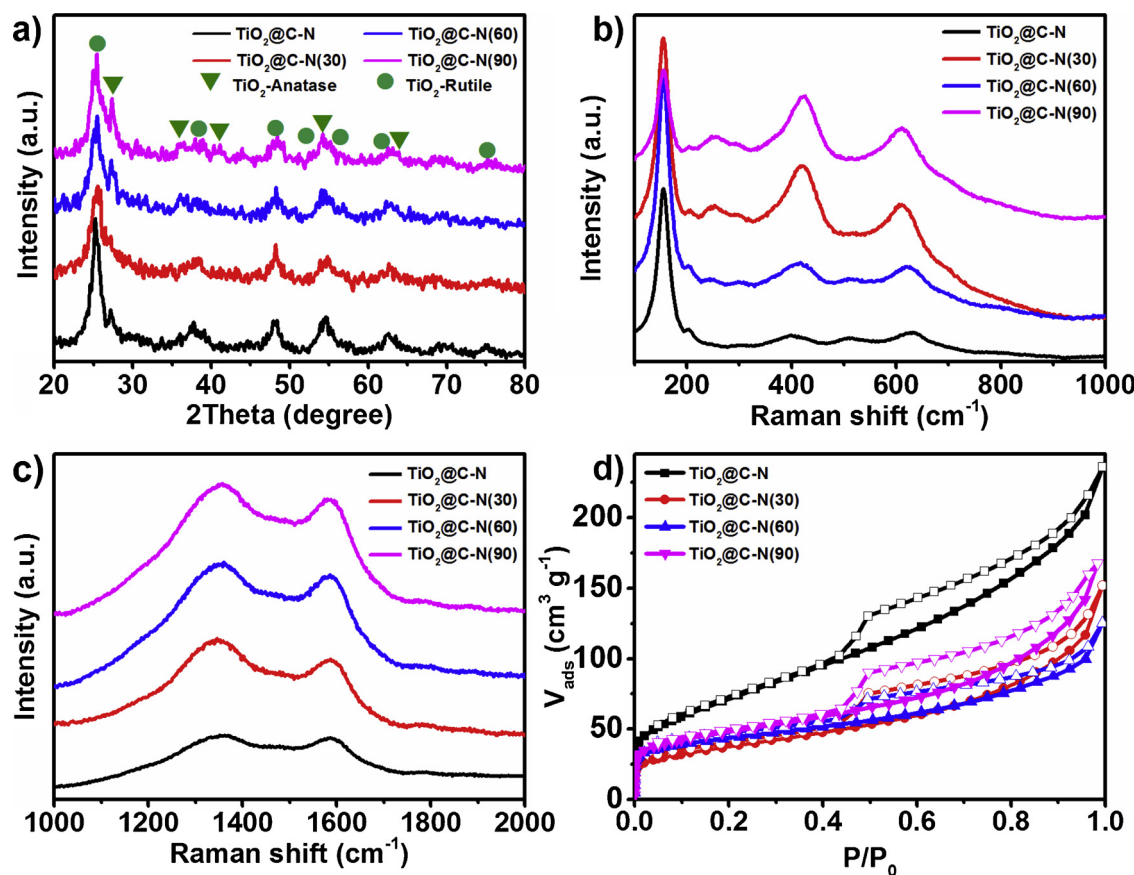


Fig. 1. XRD patterns (a), Raman spectra in the range of 100–1000 cm^{−1} (b) and 1000–2000 cm^{−1} (c), N₂ adsorption–desorption isotherms (d) of the TiO₂@C-N and TiO₂@C-N(x) samples.

Additionally, two Raman peaks located at around 1355 (D band) and 1596 cm^{−1} (G band) were also observed for graphitized carbon and the results are shown in Fig. 1c, which are ascribed to the defect sites caused by disordered sp³ carbon and the in-plane bond-stretching vibration of aromatic carbon rings, respectively [45]. The relative ratio of D band to G band (I_D/I_G) of the TiO₂@C-N, TiO₂@C-N(30), TiO₂@C-N(60), TiO₂@C-N(90) samples were 1.06, 1.26, 1.11 and 1.13, respectively, demonstrating that the degree of graphitization were enhanced with the increase of CO₂ annealing time. The improved I_D/I_G ratio would be related to the decomposition of the amorphous carbon from the TiO₂@C-N carbon matrix by CO₂ oxidation under high temperature. Given that CO₂ gas could act as an activating agent to tailor the pore morphology of carbon materials, in which normally involves the oxidation of less stable carbon from the carbon matrix to enlarge the existing pores and/or create new pores, and thus usually accompanying the reduce of specific surface area [46,47]. In order to verify the above speculation, the specific surface areas and porosities were also evaluated by N₂ adsorption–desorption measurement at 77 K (Fig. 1d and Table S1). The isotherms of all TiO₂@C-N(x) samples displayed a similar IV curve with hysteresis loop, indicating their all dominating mesoporous structure. As expected, with the introduction of CO₂ gas during the annealing process, both the BET surface area and pore volume decreased but the BJH pore size apparently increased as compared with the TiO₂@C-N sample. Moreover, the contents of C element gradually decreased with an increase in the CO₂ annealing time from 30 to 90 min (Table S2), further confirming the decomposition of partial carbon with CO₂ treatment. The improved crystallization degree of graphitic carbon in the TiO₂@C-N(x) samples and the enlarged pore size could pose positive effects to obtain both faster charge transfer and more facile diffusion chance of reactants, thus promising higher photocatalytic activity.

The surface morphologies and structure of the as-synthesized samples were also observed by SEM and TEM. The pristine NH₂-MIL-125 displayed a typical caly shape (Fig. 2a). After annealing NH₂-MIL-125 at 600 °C under Ar, the obtained TiO₂@C-N inherited the morphology of its matrix MOF but a slight shrinkage with a rougher surface, implying the decomposition and carbonization of the MOF. After the CO₂ treatment, the morphology and size of TiO₂@C-N(30) were still consistent with TiO₂@C-N sample, indicating the introduction of CO₂ did not affect the framework morphology of TiO₂@C-N. EDX elemental mapping (Fig. 2) also revealed C, N, O and Ti elements with a uniform distribution in the TiO₂@C-N(30) surface. In order to distinctly visualize the differences among the TiO₂@C-N(x) samples, high-resolution transmission electron microscopy (HRTEM) was also performed. As shown in Figs. 3 and S3, the TiO₂ nanoparticles were unevenly dispersed in the TiO₂@C-N with a mean size of 3.9 ± 0.97 nm and no significant aggregation was observed, which could be attributed to the confinement effect offered by outer carbon shell originated from the carbonization of NH₂-MIL-125. The lattice spacing of TiO₂ nanoparticle in TiO₂@C-N sample was 0.33 nm, corresponding to the (101) planes of the anatase TiO₂. Interestingly, the size of the TiO₂ nanoparticles in the TiO₂@C-N(30) sample was 3.8 ± 0.90 nm, implying that the size and dispersion of the TiO₂ nanoparticles were well preserved without appreciable change after the treatment of CO₂ annealing. However, the latter spacing of the TiO₂ nanoparticles in the TiO₂@C-N(30) sample was changed to 0.341 nm (Fig. 3f), which would be relevant to the emergence of the (110) planes of rutile transformed from anatase TiO₂ with CO₂ treatment. Furthermore, the edge of the graphene could be observed around the surface of TiO₂ nanoparticles, suggesting probably existing an interface interaction between graphene and TiO₂.

The optical absorption properties of TiO₂@C-N and all the TiO₂@C-N(x) samples were investigated using a UV-vis diffuse reflectance

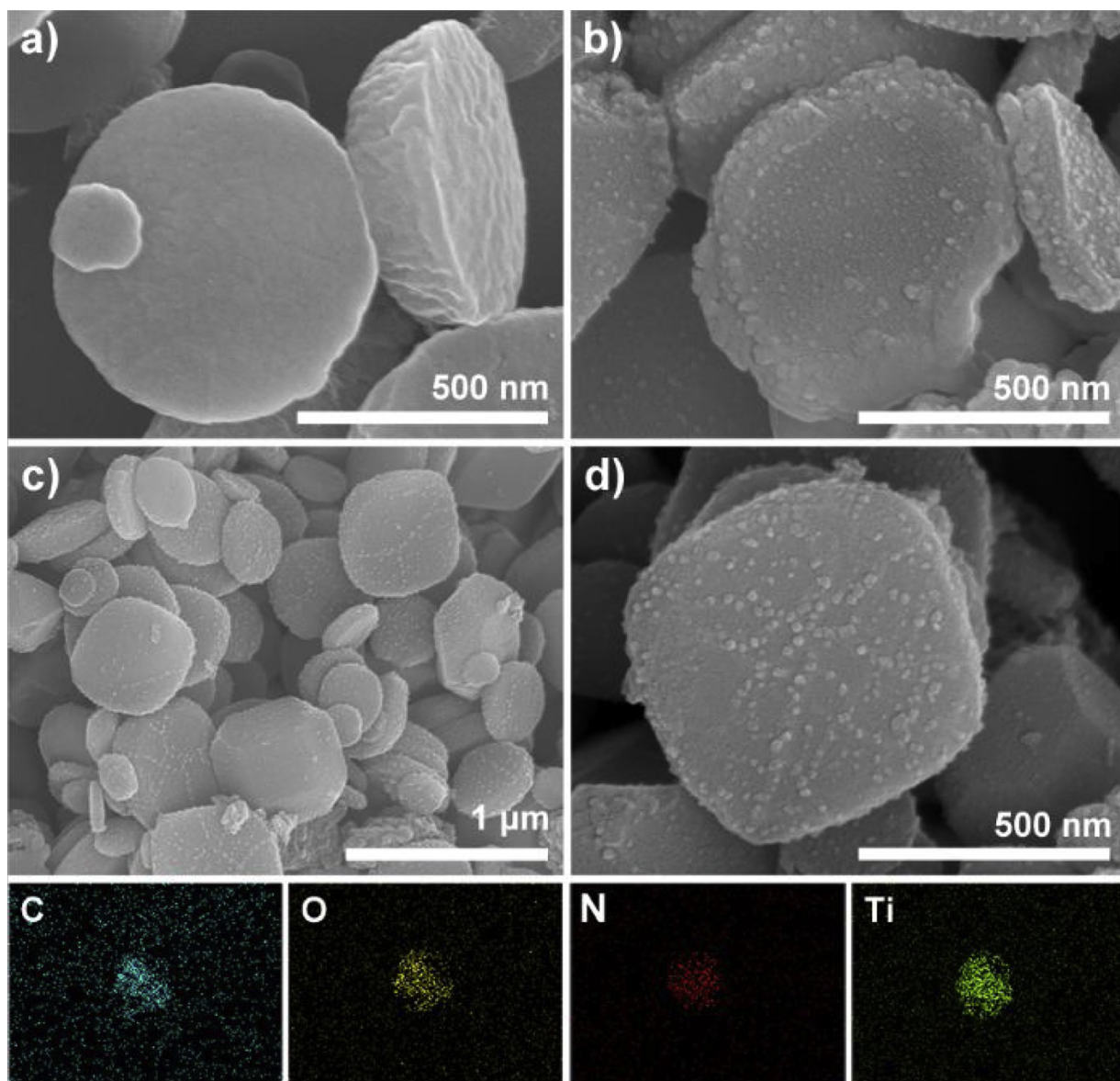


Fig. 2. SEM image of NH₂-MIL-125 (a), TiO₂@C-N (b), TiO₂@C-N(30) (c,d) and the corresponding EDS element-mapping.

spectroscopy. As shown in Fig. S4, the TiO₂@C-N sample exhibited an apparent absorption in the region of 200–270 nm, which can be attributed to the electron excitation of TiO₂ from valence band to conduction band. Additionally, a stronger absorption band in the region of 270–800 nm was found, possibly caused by the black color and carbon dopant [25,48,49]. After CO₂ annealing, the TiO₂@C-N(x) samples still displayed a similar absorption band position with TiO₂@C-N. Interestingly, the absorption intensity of all the TiO₂@C-N(30), TiO₂@C-N (60) and TiO₂@C-N(90) was enhanced drastically compared with TiO₂@C-N. Considered the phase transformation and the better interfacial contact between the TiO₂ and carbon layers, excellent synergistic effect between TiO₂ phase junction and carbon layer would be created during the CO₂ treatment process, which was beneficial to reduce the energy of electron transition and increased the light absorption.

3.2. Photocatalytic performance evaluation

Gaseous styrene, a typical aromatic VOC, was selected as a model substrate to investigate photocatalytic oxidation performance of TiO₂@C-N(x) under visible light illumination. The reactions were carried out in a continuous flow mode with a flow rate of 60 mL min⁻¹ and

involved both the dark adsorption equilibrium test and the subsequent irradiation for photocatalytic degradation. As shown in Fig. 4, the outlet styrene concentration sharply decreased to < 10% within 15 min and began to rise smoothly until 240 min in the presence of TiO₂@C-N, but the complete breakthrough time reached to ca. 820 min, demonstrating that the TiO₂@C-N sample possessed excellent adsorption capacity toward styrene. Nevertheless, after the introduction of CO₂ annealing, the adsorption capacity of styrene slightly declined despite their bigger pore sizes compared with TiO₂@C-N, which would be correlated with their lower BET surface area.

After the dark adsorption equilibrium was accomplished, the lamp was turned on to initiate the photocatalytic degradation test. In the absence of photocatalyst, only < 2% degradation of styrene was obtained under the investigated reaction conditions (Fig. S5), indicating that the effect of direct photolysis could be negligible in this system. Comparatively, in the presence of TiO₂@C-N, 55.1 ppmv of CO₂ was produced at 31.0% styrene degradation within 240 min of visible-light irradiation (Fig. 5), corresponding to the mineralization efficiency of 19.7%. When the TiO₂@C-N(30) was employed, the degradation efficiency of styrene was enhanced to 62.4% and the styrene mineralization rate was reached to 51.9% within 240 min. Moreover, the TiO₂@C-

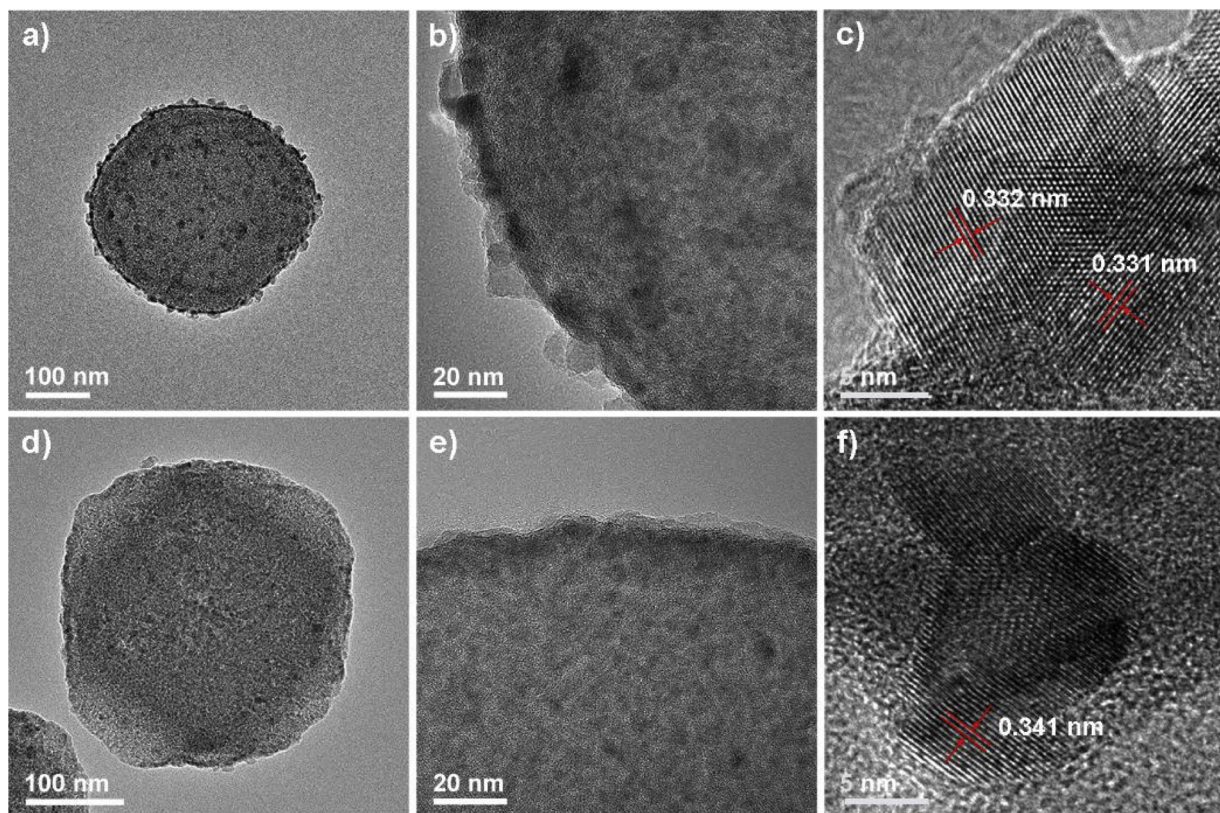


Fig. 3. TEM image of $\text{TiO}_2@\text{C-N}$ (a–c) and $\text{TiO}_2@\text{C-N}(30)$ (d–f) samples.

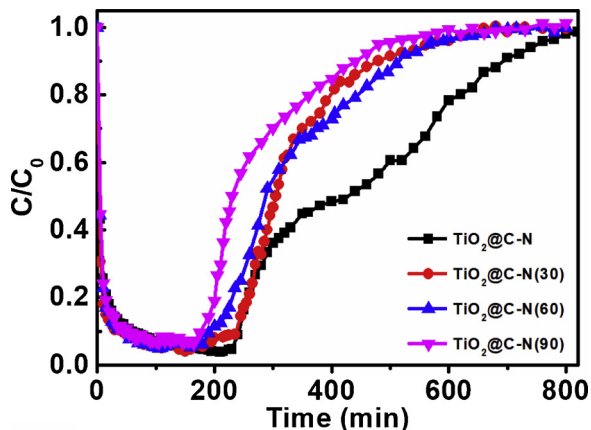


Fig. 4. Adsorption kinetic curves of styrene by the $\text{TiO}_2@\text{C-N}$ and $\text{TiO}_2@\text{C-N}(x)$ samples.

$\text{N}(x)$ with CO_2 annealing time of 60 and 90 min also worked smoothly in these photocatalytic oxidation reactions, displaying a 55.9% styrene degradation efficiency with 45.3% mineralization efficiency and 41.5% styrene degradation efficiency with 33.9% mineralization efficiency for both photocatalysts, respectively. The above results demonstrated that the $\text{TiO}_2@\text{C-N}$ with CO_2 annealing could drastically promoted the degradation and mineralization reactions, and the $\text{TiO}_2@\text{C-N}(30)$ exhibited the optimized photocatalytic activity.

It should be noted that both the evolution curves of photocatalytic degradation and formed CO_2 for the $\text{TiO}_2@\text{C-N}$, and all the $\text{TiO}_2@\text{C-N}(x)$ samples appeared a roll-up phenomenon, which instantly raised upon switching on the lamp and then gradually decreased to a stable level. This phenomenon might be associated with their high equilibrium adsorption amount toward styrene. When the lamp was switched on, the abundant adsorbed styrene could be swiftly desorbed and

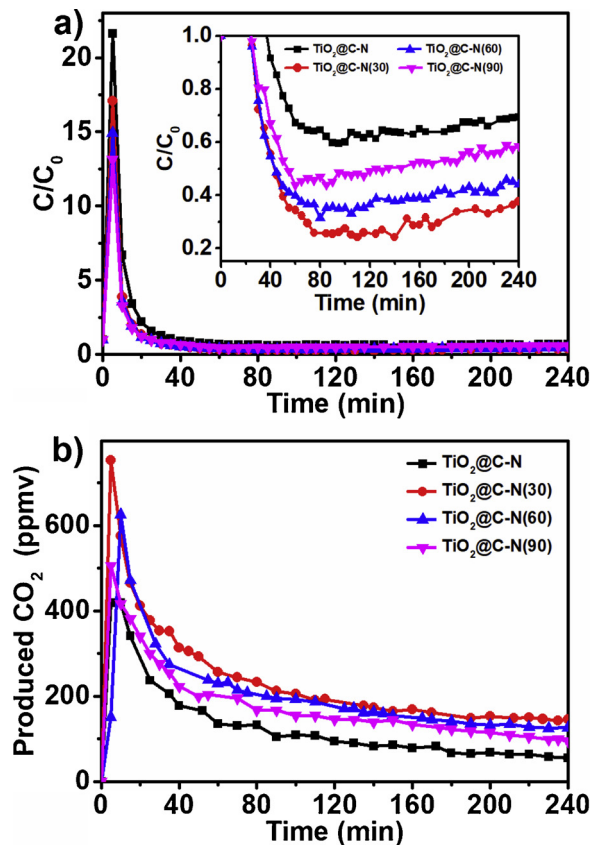


Fig. 5. Evolution of styrene (a) and formed CO_2 (b) during the photocatalytic oxidation reaction by $\text{TiO}_2@\text{C-N}$ and $\text{TiO}_2@\text{C-N}(x)$ composites.

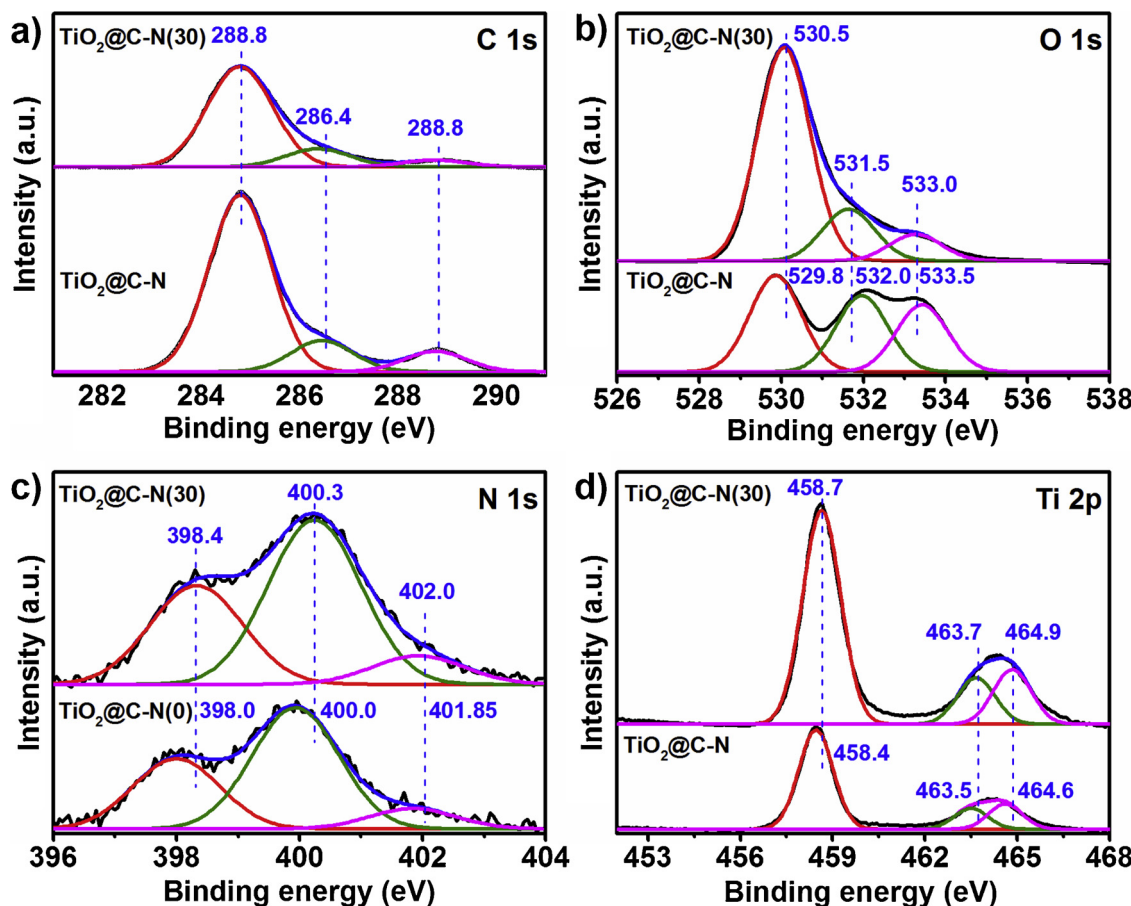


Fig. 6. XPS spectra of C 1s (a), O 1s (b), N 1s (c) and Ti 2p (d) for TiO₂@C-N and TiO₂@C-N(30) samples, respectively.

released from the surface of photocatalyst before being quickly degraded due to heat generation under light irradiation [7,50]. Strikingly, an extremely high styrene concentration ($C/C_0 = 21.6$) was detected at the outlet of reactor for the TiO₂@C-N photocatalyst, and about 1.3 and 1.5 times higher concentration than that of TiO₂@C-N(30) and TiO₂@C-N(60) was obtained, respectively. However, the amount of formed CO₂ by the TiO₂@C-N(30) and TiO₂@C-N(60) samples were 2.6 and 2.3 times higher than that of the TiO₂@C-N. These results implied that the introduction of CO₂ annealing procedure could significantly improve both the degradation and mineralization efficiency.

To reveal the reasons for the remarkable activity differences between the TiO₂@C-N and TiO₂@C-N(x) materials, XPS and EPR were also employed to probe their electron structure features and chemical state information. The full survey and high-resolution XPS spectra of the TiO₂@C-N and TiO₂@C-N(30) samples were presented in Figs. S6 and 6, respectively. Only the C, N, O and Ti elements were detected in both the TiO₂@C-N and TiO₂@C-N(30) samples (Fig. S6). As depicted in Fig. 6a, the characteristic peak at 284.8 eV can be correlated with pure graphitic sp² carbon while the other peaks at 286.4 and 288.8 eV were ascribed to N–C and/or Ti–C interactions and C=O bonds, respectively [51,52]. Moreover, the peak positions of the above peaks were almost identical for both TiO₂@C-N and TiO₂@C-N(30) samples, indicating that the introduction of CO₂ annealing did not alter the surface oxygen species of samples. Nevertheless, an apparent increase in relative content of N–C and/or Ti–C bonds and a decrease in the relative content of C=O bonds of TiO₂@C-N(30) sample as compared with TiO₂@C-N were observed (Table S3). According to the high-resolution XPS spectrum of O1s for TiO₂@C-N, three peaks can be visualized, and the O²⁻ species of the TiO₂ lattice at 529.8 eV, the –OH bands at 532.0 eV, and the C–OH and/or C–O–C species at 533.5 eV were consistent with the reference [49]. After the annealing by CO₂, the

peak position of the O²⁻ species was obviously shifted to higher binding energy as compared with TiO₂@C-N. However, both the peak positions of the O–H and C–OH and/or C–O–C bands were shifted to lower binding energies accompanying a decrease in peak area (Table S4). Moreover, the content change of nitrogen species and the binding energies of both the N 1s and Ti 2p for TiO₂@C-N revealed distinct shifts originated from a change imbalance induced by the decomposition of the amorphous carbon and substitutional carbon doping in TiO₂ (Table S5) [53]. Based on the above observations, it was reasonable to conclude that CO₂ annealing could enhance the interfacial contact between the TiO₂ and carbon layers.

The separation efficiency of photogenerated electron-hole pairs play crucial role in determining the photocatalytic performance. Thus, the photocurrent response tests were also carried out under visible light irradiation to further evidence the charge separation efficiencies (Fig. 7a). The TiO₂@C-N(30) and TiO₂@C-N(60) exhibited much higher photocurrent density compared with both TiO₂@C-N and TiO₂@C-N(90). Strikingly, an obviously anodic spike was observed in the transient photocurrent curves of both the TiO₂@C-N(30) and TiO₂@C-N(60) samples. The remarkably improved photocurrent density and anodic spike revealed that the CO₂ annealing could outstandingly accelerate the separation efficiencies of photoexcited carriers [7,54]. Furthermore, these conclusions were also confirmed by the EIS test results (Fig. 7b), in which TiO₂@C-N presented the biggest radius. After the introduction of CO₂ annealing, the arc radius of TiO₂@C-N(x) samples were distinctly shortened and the TiO₂@C-N(30) exhibited the smallest radius. These results further validated that the interfacial charge transfer and the separation of photoexcited carriers could be dramatically boosted due to the emergence of excellent interfacial interaction and appropriate phase transformation after CO₂ annealing. Thus, the substantial differences in both the interfacial charge transfer and photogenerated

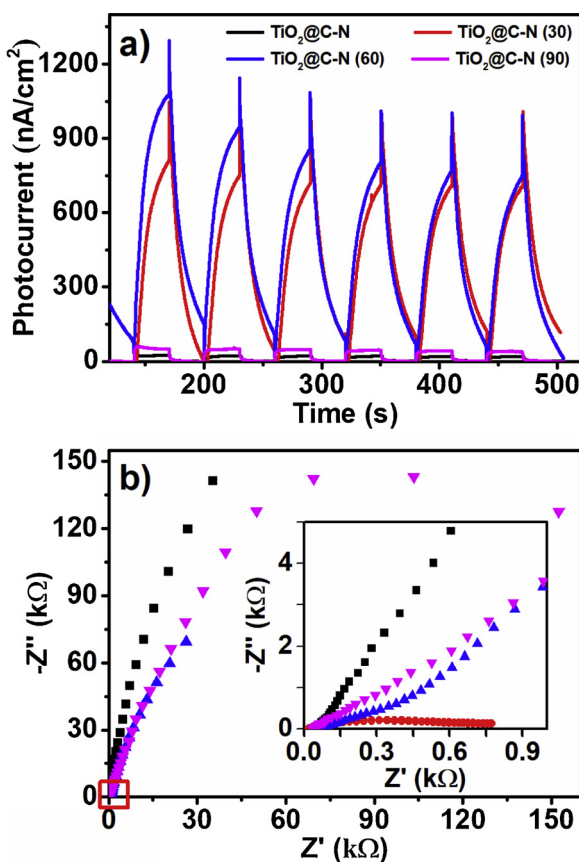


Fig. 7. Photocurrent responses (a) and EIS Nyquist plots (b) and UV-vis diffuse reflectance spectra (c) of the TiO₂@C-N and TiO₂@C-N(x) samples.

electron-hole separation of the TiO₂@C-N and TiO₂@C-N(x) samples would be responsible for their different photocatalytic activity.

3.3. Identification of reactive oxygen species and photocatalytic degradation mechanism of styrene

To reveal the superior photocatalytic reactivity and higher mineralization efficiencies obtained of the TiO₂@C-N(x) samples, a possible degradation intermediates were measured and the reaction mechanism were also proposed. Given that the photocatalytic degradation process usually involved two key steps of an occurrence of active radicals and following catalytic decomposing of styrene, the formed active radicals and potential intermediates should be investigated. With this consideration, the important reactive oxygen species (i.e. ·O₂⁻, ·OH) generated in the photocatalytic reaction were detected by EPR spectroscopy using DMPO as spin trapping reagent (Fig. 8). In the absence of photocatalyst, almost no signals of ·O₂⁻ and ·OH radicals could be detected. When the TiO₂@C-N sample was employed, the trapped ·O₂⁻ signal was still difficult to observe. However, the TiO₂@C-N(30) exhibited apparently strong characteristic sextet peaks of DMPO-·O₂⁻ adduct, suggesting that TiO₂@C-N(30) possessed excellent capability for the generation of ·O₂⁻ during the photocatalytic process and the results was also similar with the reference [55]. It is widely accepted that the ·O₂⁻ radical is formed via the reduction of adsorbed O₂ by conduction band e⁻ [55–58]. As demonstrated by Raman and XPS measurements, the TiO₂@C-N(30) sample had a stronger interface interaction between TiO₂ and its outer carbon compared to TiO₂@C-N, which was favorable for the transfer of conduction band e⁻ from TiO₂ to carbon. Additionally, it had been demonstrated that the heterojunction located at the anatase/rutile phase junction could improve effectively transfer efficiency of photoexcited electron by prolonging

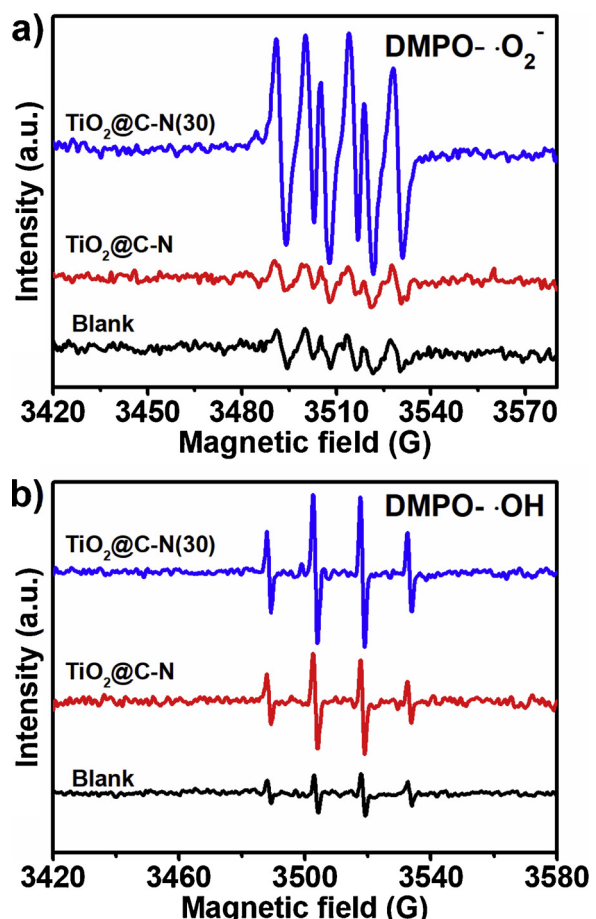
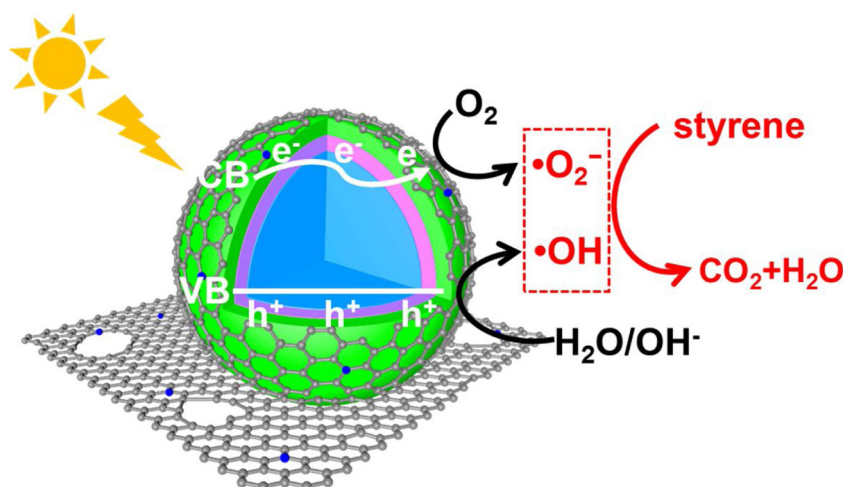


Fig. 8. DMPO spin-trapping EPR spectra recorded at ambient temperature in the presence of TiO₂@C-N and TiO₂@C-N (30) for DMPO-·O₂⁻ formed in irradiated methanol dispersion (a), and DMPO-·OH formed in irradiated H₂O dispersion (b).

electron lifetimes in mixed phase TiO₂ [12–16,59]. Moreover, the TiO₂@C-N(30) sample possessed excellent anatase/rutile TiO₂ phase junction compared with the TiO₂@C-N. As a consequence, the synergistic effect between mixed phase junction TiO₂ and its outer carbon shell would guarantee the rapid transfer of electron from TiO₂ to photocatalyst surface to react with O₂ (Scheme 2), thereby promoting the generation of abundant ·O₂⁻ radicals on the TiO₂@C-N(30) under visible light irradiation. Simultaneously, more photogenerated holes (h⁺) will be remained in the valence band of TiO₂, which could further react with the surface hydroxyl groups on TiO₂ to form highly reactive ·OH [55,57,58]. The above processes should allow more efficient photogenerated electron transfer and separation of electron-hole pairs, which also supported by the results of photoelectrochemical measurements. Moreover, it can be clearly found that the intensity of DMPO-·OH adducts over TiO₂@C-N(30) was much stronger than that of TiO₂@C-N (Fig. 8b), validating that more ·OH radicals were produced for TiO₂@C-N(30) photocatalyst. Subsequently, the produced ·O₂⁻ and ·OH radicals as main reactive oxygen species would preferentially attack the vinyl group of styrene due to lower barrier energies according to the reference [8], resulting in epoxidation and/or bond rupture of styrene. Then, these intermediates were further converted into by-products such as benzene, benzaldehyde, acetaldehyde and formaldehyde (Fig. S7 and Table S6) which can be well monitored by means of PTR-ToF-MS, and eventually decomposed into CO₂ and H₂O with the help of the oxidation reaction of ·O₂⁻ and ·OH radicals.



Scheme 2. Possible reaction mechanism for the photocatalytic oxidation of styrene over $\text{TiO}_2@\text{C-N}(\text{x})$ nanocomposites.

4. Conclusions

In summary, a facile strategy was developed to construct the N-doped mesoporous carbon confined anatase-rutile phase junction TiO_2 composites via direct pyrolysis of $\text{NH}_2\text{-MIL-125}$ under Ar and subsequent CO_2 atmosphere. The inert Ar atmosphere offered a benign environment for pyrolyzing MOF to form $\text{TiO}_2@\text{C-N}$. Subsequently, the weak oxidative CO_2 served as an anatase-rutile phase transformation promoter and favored decomposing the amorphous carbon of $\text{TiO}_2@\text{C-N}$ to improve the ratio of graphitic carbon. Highly graphitized N-doped mesoporous carbon wrapping on the surface of TiO_2 enhanced interfacial contact between TiO_2 and carbon, thus improving the absorption ability to visible light and accelerating the photogenerated electron transfer. Moreover, the formed anatase-rutile TiO_2 phase junction in the $\text{TiO}_2@\text{C-N}(\text{x})$ samples could decrease the possibility of recombination of electron-hole pairs by offering fast electron transfer channel. Under the synergistic effect of the strong interface interaction between TiO_2 and its outer highly graphitized carbon shell as well as the formed anatase-rutile phase junction, $\text{TiO}_2@\text{C-N}(\text{x})$ generated significantly stronger oxidative $\cdot\text{O}_2^-$ and $\cdot\text{OH}$ radicals than $\text{TiO}_2@\text{C-N}$, thus exhibiting remarkably superior photocatalytic activity and high mineralization efficiency in gaseous-phase oxidation of styrene under visible light irradiation. The utilization of easily available MOFs as starting materials and low cost CO_2 as both phase transformation agent and mild oxidant as well as excellent photocatalytic performance make the photocatalytic system more green and sustainable. Moreover, the pyrolysis strategy is a common method in largescale production of various commercial products. These advantages endow the proposed photocatalyst synthesis strategy highly feasible for larger-scale fabrication. This work not only puts forward a new strategy for the preparation of advanced nanocomposites derived from MOFs, but also extends the application of MOF in photocatalytic degradation of VOC air pollution.

Acknowledgments

This work was supported by National Natural Science Foundation of China (21406075, 41425015, and 41731279), Local Innovative and Research Teams Project of Guangdong Pearl River Talents Program (2017BT01Z032), Pearl River S&T Nova Program of Guangzhou (201806010177), Guangdong Special Support Plan for Science and Technology for Innovation leading scientists (2016TX03Z094 and 2016TQ03Z291) and the Innovation Team Project of Guangdong Provincial Department of Education (2017KCXTD012).

Appendix A. Supplementary data

Supplementary material related to this article can be found, in the online version, at doi:<https://doi.org/10.1016/j.apcatb.2019.03.054>.

References

- [1] E. Barea, C. Montoro, J.A.R. Navarro, Chem. Soc. Rev. 43 (2014) 5419–5430.
- [2] M. Hakim, Y.Y. Broza, O. Barash, N. Peled, M. Phillips, A. Amann, H. Haick, Chem. Rev. 112 (2012) 5949–5966.
- [3] A.H. Mamaghani, F. Haghighat, C.-S. Lee, Appl. Catal. B-Environ. 203 (2017) 247–269.
- [4] T.C. An, J.Y. Chen, X. Nie, G.Y. Li, H.M. Zhang, X.L. Liu, H.J. Zhao, ACS. Appl. Mater. Inter. 4 (2012) 5988–5996.
- [5] Z. Shayegan, C.S. Lee, F. Haghighat, Chem. Eng. J. 334 (2018) 2408–2439.
- [6] S. Weon, E. Choi, H. Kim, J.Y. Kim, H.-J. Park, S.-m. Kim, W. Kim, W. Choi, Environ. Sci. Technol. 52 (2018) 9330–9340.
- [7] P. Yao, H. Liu, D. Wang, J. Chen, G. Li, T. An, J. Colloid Interface Sci. 522 (2018) 174–182.
- [8] H. Wang, Y. Ji, J. Chen, G. Li, T. An, Sci. Rep. 5 (2015) 15059.
- [9] H. Wang, T. Yu, X. Tan, H. Zhang, P. Li, H. Liu, L. Shi, X. Li, J. Ye, Ind. Eng. Chem. Res. 55 (2016) 8096–8103.
- [10] J.Y. Chen, G.Y. Li, H.M. Zhang, P.R. Liu, H.J. Zhao, T.C. An, Catal. Today 224 (2014) 216–224.
- [11] Y.J. Shu, J. Ji, Y. Xu, J.G. Deng, H.B. Huang, M. He, D.Y.C. Leung, M.Y. Wu, S.W. Liu, S.L. Liu, G.Y. Liu, R.J. Xie, Q.Y. Feng, Y.J. Zhan, R.M. Fang, X.G. Ye, Appl. Catal. B-Environ. 220 (2018) 78–87.
- [12] Y. Gao, J. Zhu, H. An, P. Yan, B. Huang, R. Chen, F. Fan, C. Li, J. Phys. Chem. Lett. 8 (2017) 1419–1423.
- [13] W. Fu, G. Li, Y. Wang, S. Zeng, Z. Yan, J. Wang, S. Xin, L. Zhang, S. Wu, Z. Zhang, Chem. Commun. 54 (2017) 58–61.
- [14] Z. Luo, A.S. Poyraz, C.-H. Kuo, R. Miao, Y. Meng, S.-Y. Chen, T. Jiang, C. Wenos, S.L. Suib, Chem. Mater. 27 (2014) 6–17.
- [15] D. Shingai, Y. Ide, W.Y. Sohn, K. Katayama, Phys. Chem. Chem. Phys. 20 (2018) 3484–3489.
- [16] X. Wang, C. Li, J. Phys. Chem. C 122 (2018) 21083–21096.
- [17] Q. Tay, X. Wang, X. Zhao, J. Hong, Q. Zhang, R. Xu, Z. Chen, J. Catal. 342 (2016) 55–62.
- [18] X. Li, J.G. Yu, S. Wageh, A.A. Al-Ghamdi, J. Xie, Small 12 (2016) 6640–6696.
- [19] L.K. Putri, W.J. Ong, W.S. Chang, S.P. Chai, Appl. Surf. Sci. 358 (2015) 2–14.
- [20] L. Jing, W. Zhou, G. Tian, H. Fu, Chem. Soc. Rev. 42 (2013) 9509–9549.
- [21] Y. Zhang, Z. Tang, X. Fu, Y. Xu, ACS Nano 4 (2010) 7303–7314.
- [22] A. Ziarati, A. Badiei, R. Luque, Appl. Catal. B-Environ. 240 (2019) 72–78.
- [23] G.Y. Li, X. Nie, J.Y. Chen, Q. Jiang, T.C. An, P.K. Wong, H.M. Zhang, H.J. Zhao, H. Yamashita, Water Res. 86 (2015) 17–24.
- [24] G.Y. Li, X. Nie, Y.P. Gao, T.C. An, Appl. Catal. B-Environ. 180 (2016) 726–732.
- [25] X. Li, J. Yu, S. Wageh, A.A. Al-Ghamdi, J. Xie, Small 12 (2016) 6640–6696.
- [26] M. Li, D. Li, M. O'Keeffe, O.M. Yaghi, Chem. Rev. 114 (2014) 1343–1370.
- [27] M. Wen, K. Mori, Y. Kuwahara, T. An, H. Yamashita, Appl. Catal. B-Environ. 218 (2017) 555–569.
- [28] Y.Z. Chen, R. Zhang, L. Jiao, H.L. Jiang, Coordin. Chem. Rev. 362 (2018) 1–23.
- [29] S. Dang, Q.L. Zhu, Q. Xu, Nat. Rev. Mater. 3 (2018) 17075.
- [30] R. Fang, P. Tian, X. Yang, R. Luque, Y. Li, Chem. Sci. 9 (2018) 1854–1859.
- [31] C. Bai, A. Li, X. Yao, H. Liu, Y. Li, Green Chem. 18 (2016) 1061–1069.
- [32] K. Nakatsuka, T. Yoshii, Y. Kuwahara, K. Mori, H. Yamashita, Chem-Eur. J. 24 (2018) 898–905.
- [33] S. Liu, M. Tong, G. Liu, X. Zhang, Z. Wang, G. Wang, W. Cai, H. Zhang, H. Zhao,

- Inorg. Chem. Front. 4 (2017) 491–498.
- [34] A. Li, Z. Wang, H. Yin, S. Wang, P. Yan, B. Huang, X. Wang, R. Li, X. Zong, H. Han, C. Li, Chem. Sci. 7 (2016) 6076–6082.
- [35] F. Wang, J.H. Ho, Y. Jiang, R. Amal, ACS Appl. Mater. Interfaces 7 (2015) 23941–23948.
- [36] Y. Fu, D. Sun, Y. Chen, R. Huang, Z. Ding, X. Fu, Z. Li, Angew. Chem. Int. Ed. 51 (2012) 3364–3367.
- [37] J. Zhao, R.Y. Zhang, Atmos. Environ. 38 (2004) 2177–2185.
- [38] A. Gandolfo, S. Marque, B. Temime-Roussel, R. Gemayel, H. Wortham, D. Truffier-Boutry, V. Bartolomei, S. Gligorovski, Environ. Sci. Technol. 52 (2018) 11328–11337.
- [39] B. Yuan, A.R. Koss, C. Warneke, M. Coggon, K. Sekimoto, J.A. de Gouw, Chem. Rev. 117 (2017) 13187–13229.
- [40] Y. Shi, D. Yang, R. Yu, Y. Liu, J. Qu, B. Liu, Z.-Z. Yu, ACS Appl. Energy Mater. 1 (2018) 4186–4195.
- [41] F. Tian, Y. Zhang, J. Zhang, C. Pan, J. Phys. Chem. C 116 (2012) 7515–7519.
- [42] O. Frank, M. Zukalova, B. Laskova, J. Kurti, J. Koltaib, L. Kavan, Phys. Chem. Chem. Phys. 14 (2012) 14567–14572.
- [43] G.A.B.G.A. Tompsett, R.P. Cooney, J.B. Metson, K.A. Rodgers, J.M. Seakins, J. Raman Spectrosc. 26 (1995) 57–62.
- [44] H.T.T. Tran, H. Kosslick, M.F. Ibad, C. Fischer, U. Bentrup, T.H. Vuong, L.Q. Nguyen, A. Schulz, Appl. Catal. B-Environ. 200 (2017) 647–658.
- [45] F. Banhart, J. Kotakoski, A.V. Krasheninnikov, ACS Nano 5 (2011) 26–41.
- [46] J. Alvarez, G. Lopez, M. Amutio, J. Bilbao, M. Olazar, Ind. Eng. Chem. Res. 54 (2015) 7241–7250.
- [47] S.E. Chun, J. Choi, J.F. Whitacre, Ionics 24 (2018) 2055–2061.
- [48] C. Yang, X. Zhang, J. Qin, X. Shen, R. Yu, M. Ma, R. Liu, J. Catal. 347 (2017) 36–44.
- [49] S.Y. Pu, R.X. Zhu, H. Ma, D.L. Deng, X.J. Pei, F. Qi, W. Chu, Appl. Catal. B-Environ. 218 (2017) 208–219.
- [50] D. Luo, M.S. Hasan, S. Shahid, B.N. Khlebtsov, M.J. Cattell, G.B. Sukhorukov, Langmuir 33 (2017) 7982–7993.
- [51] Z. Guo SrinivasGadipelli, ChemSusChem 8 (2015) 2123–2132.
- [52] S. Zhang, Y. Cai, H. He, Y. Zhang, R. Liu, H. Cao, M. Wang, J. Liu, G. Zhang, Y. Li, H. Liu, B. Li, J. Mater. Chem. A 4 (2016) 4738–4744.
- [53] J. Qin, J. Catal. 347 (2017) 36–44.
- [54] D. Jiang, W. Wang, L. Zhang, Y. Zheng, Z. Wang, ACS Catal. 5 (2015) 4851–4858.
- [55] C. Chen, W. Ma, J. Zhao, Chem. Soc. Rev. 39 (2010) 4206–4219.
- [56] Y. Nosaka, A.Y. Nosaka, Chem. Rev. 117 (2017) 11302–11336.
- [57] J.C. Colmenares, R. Luqu, Chem. Soc. Rev. 43 (2014) 765–778.
- [58] M. Ponczek, C. George, Environ. Sci. Technol. 52 (2018) 5191–5198.
- [59] S. Shen, X. Wang, T. Chen, Z. Feng, C. Li, J. Phys. Chem. C 118 (2014) 12661–12668.